

Volume-Consistent Kneading-Based Deformation Manufacturing for Material-Efficient Shaping

Li Lei^{a,*}, Gong Jiale^{b,*}, Li Ziyang^a, Wang Hong^{a,**}

^a*School of Mechanical Engineering and Automation, Northeastern University, Shenyang, 110819, China*

^b*Future Laboratory, Tsinghua University, Beijing, 100084, China*

Abstract

Conventional subtractive manufacturing inevitably involves material loss during geometric realization, while additive manufacturing still suffers from limitations in surface quality, process continuity, and productivity when fabricating complex geometries. To address these challenges, this paper proposes a volume-consistent kneading-based forming method for plastic materials, enabling continuous and controllable three-dimensional deformation under mass conservation. An integrated kneading-based manufacturing system is developed, in which geometry-aware kneading command generation, layer-wise kneading execution, and in-process point-cloud scanning are tightly coupled to form a closed-loop workflow of scanning, forming, and feedback compensation. Target geometries are analyzed through layer-wise point-cloud processing and classified into enveloping and non-enveloping types. Accordingly, an Envelope Shaping First strategy and a Similar Gradient Method are adopted to ensure stable material flow and continuous deformation. An RMSE-based compensation scheme is further introduced to correct systematic geometric deviations induced by elastic rebound and material redistribution. Experimental validation on five representative geometries demonstrates high geometric fidelity, with material utilization consistently exceeding 98%. The results indicate that kneading-based forming provides a promising alternative manufacturing paradigm for low-waste, customizable production.

Keywords: Kneading-based forming, Volume-consistent, manufacturing,

*These authors contributed equally to this work.

**Corresponding author.

URL: hongwang@mail.neu.edu.cn (Wang Hong)

1. Introduction

Manufacturing systems have evolved from craft-oriented production to highly systematized and customization-oriented paradigms [1], where digitalization and flexibility increasingly reshape how manufacturing tasks are organized and optimized [2]. Within this landscape, subtractive manufacturing remains a mature and widely deployed mechanism for geometric realization through controlled material removal, and has further expanded toward robotic machining and the processing of advanced materials such as composites [3]. However, subtractive processes inherently involve material loss and potential environmental burdens; in the context of sustainable manufacturing, the trade-off between high precision and high waste becomes increasingly critical [4, 5].

Additive manufacturing significantly enlarges the feasible design space for complex components, and emerging directions such as multi-axis additive manufacturing [6] and additive manufacturing of composite materials continue to broaden its applicability [7, 8]. Nevertheless, additive processes still face practical bottlenecks, including surface quality limitations, support-structure dependency, and distortion control challenges, which collectively increase process-chain complexity and constrain productivity and energy efficiency [9, 10, 11, 12]. As a result, despite the progress of both paradigms, there remains a persistent need for a manufacturing mechanism that can achieve continuous, controllable deformation while maintaining high material efficiency.

Under the Industry 4.0 framework, interconnectivity, data, and automation have enhanced equipment capability and system integration [13]; yet, for personalized and complex products, manufacturing systems increasingly demand “controllable deformation with real-time correction” to maintain digital–physical consistency throughout production [14, 15, 16]. Digital twin technologies have been widely adopted to bridge design–process–quality information and to support knowledge modeling and in-process quality closure at the system level [17, 18, 19]. Meanwhile, error formation in equipment and processes often follows deterministic and thermal-driven mechanisms, making compensation strategies and data-driven models essential for repeatability and accuracy in integrated manufacturing workflows [20, 21, 22]. In addition, manufacturing data standards and process planning still face alignment

challenges across the “model–process–equipment” chain, which limits traceability and automation across stages [23, 24, 25].

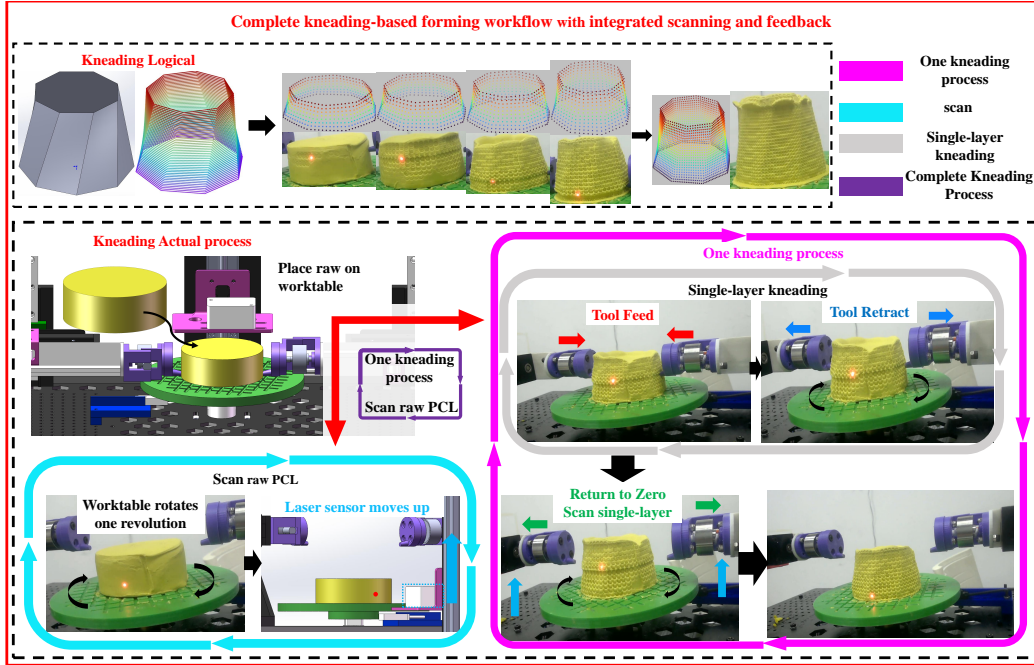


Figure 1: Complete kneading-based forming workflow with integrated scanning and feedback.

From the perspective of zero-defect and zero-waste manufacturing, non-destructive inspection and online measurement [26] provide the necessary basis for a closed-loop workflow of “detecting deviation–feedback compensation–re-manufacturing” [27, 28]. Distinct from material removal or deposition, plastic forming emphasizes controlled material flow under volume (mass) conservation, where flow laws and control directly determine the attainable geometric accuracy [29, 30, 31, 32]. In parallel, recent studies on robotic manipulation of deformable objects suggest that stability and controllability of shaping soft/plastic materials can be achieved through structural priors and planning strategies, providing inspiration for a computable and feedback-enabled volume-conserving shaping mechanism [33, 34]. To address the above challenges, this study proposes a kneading-based forming paradigm that enables continuous and controllable deformation of plastic materials under volume conservation. As illustrated in Fig. 1, the proposed manufacturing workflow integrates geometry-aware planning, layer-wise kneading execution, and

in-process scanning into a closed-loop forming system. Raw material geometry is first captured through non-destructive scanning, followed by iterative single-layer kneading and re-scanning to compensate for geometric deviations induced by material flow and elastic rebound. By tightly coupling digital geometric representation with physical forming actions, the workflow ensures digital-physical consistency while achieving high material efficiency.

2. System and 3D model design

Independently designed and built the mechanical structure, sensor system, and control system of the intelligent kneading device; developed the lower computer kneading controller software system, the upper computer software system for point cloud sampling, processing, and comparative analysis, as well as the automatic kneading instruction generation software system.

2.1. Hardware system and software system design

The lower-level control system is built around an RK3588 platform (ROCKCHIP, Fuzhou, Fujian, China), equipped with a 128 GB solid-state drive (Yangtze Memory Technologies, Wuhan, Hubei, China) and 8 GB of RAM (Samsung Electronics, Suwon, Gyeonggi-do, South Korea), and running an Ubuntu 20.04 development environment. The RK3588 communicates with a laser distance sensor (BOJKE, Shenzhen, Guangdong, China), which provides a measurement range of 80 mm, a measurement accuracy of 0.2 mm, and a maximum data acquisition frequency of 100 Hz, via the RS485 protocol (MAXIM, California, United States). In addition, the RK3588 interfaces with two Arduino Uno boards (Arduino AG, Ivrea, Italy) through serial and RS232 connections, respectively. The two Arduino boards run an improved version of the Arduino CNC firmware and are responsible for controlling five 28-stepper motors (SUHENG, YanCheng, JiangSu, China) with a step angle of 1.8° , a rated current of 0.8 A, and a holding torque of $0.08 \text{ N} \cdot \text{m}$, as well as one 57-stepper motor (YINGPENG, Shenzhen, Guangdong, China) with a step angle of 1.8° , a rated current of 4.5 A, and a holding torque of $0.5 \text{ N} \cdot \text{m}$. Position and state feedback are provided by six inductive proximity switches (SUHENG, YanCheng, JiangSu, China), which output digital signals in 1/0 mode. Four cooling fans (YIHE, PuNing, Guangdong, China) are installed to dissipate heat from the two horizontally moving 28-stepper motors. The entire system is powered by a DC switching power supply that converts

220 VAC to 24 V at 20 A (HONGMING, Zhongshan, Guangdong, China). The overall hardware architecture of the system is illustrated in Fig. 2.

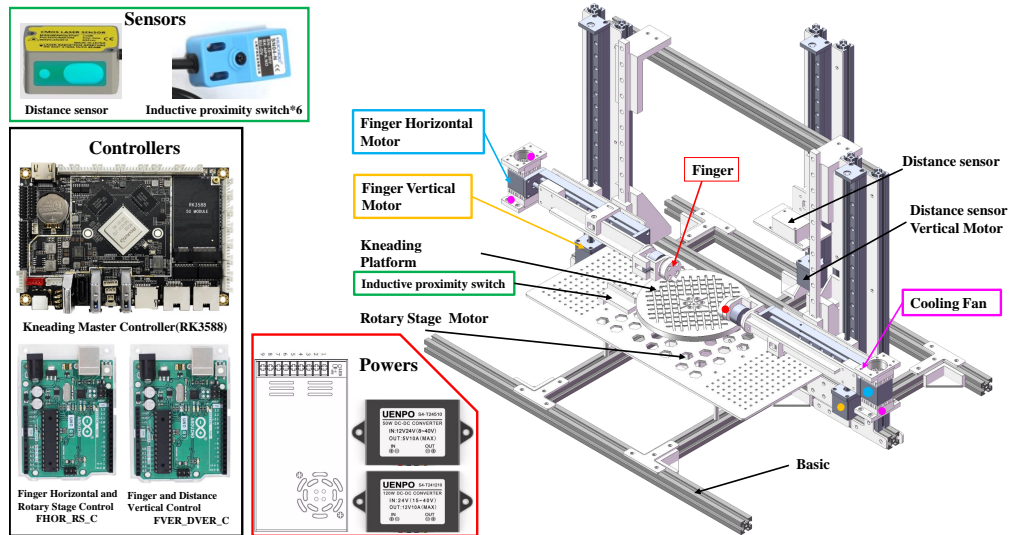


Figure 2: Hardware structure diagram

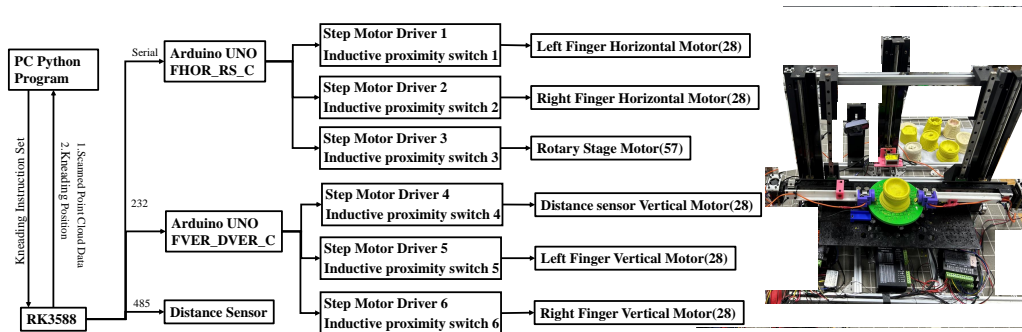


Figure 3: Control and sensor system relationship diagram

Main relationship and physical components of the kneading sensor and control system in Fig. 3. The RK3588 controls the *FHOR_RS_C* and *FVER_DVER_C* based on the “Kneading Instruction Set” received from the upper computer, using G-code commands. The *FHOR_RS_C* is responsible for controlling the horizontal movement of the left and right fingers

as well as the rotation of the rotary stage, while the $FVER_DVER_C$ controls the vertical motion of the two fingers and the distance sensor.

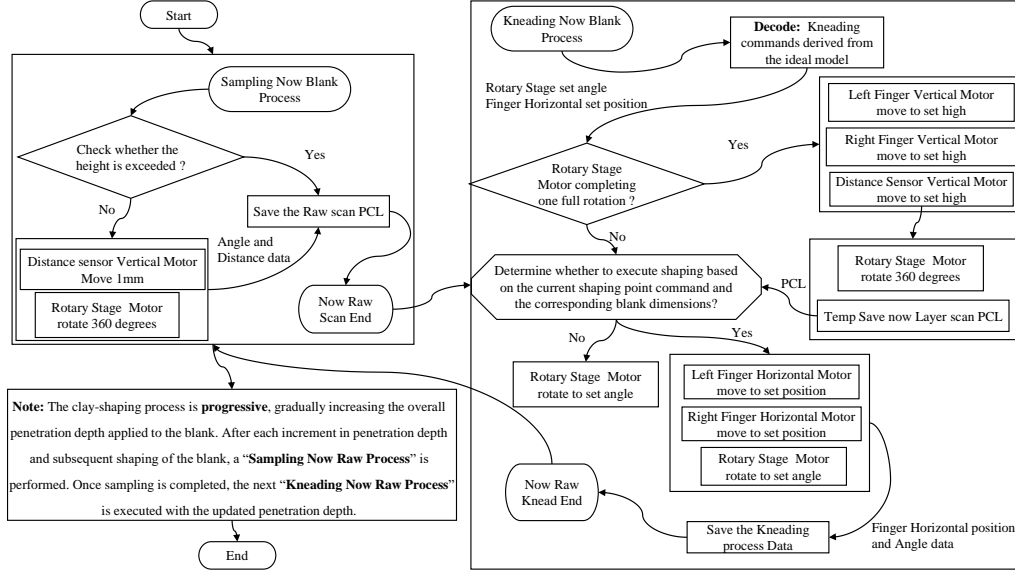


Figure 4: Control flowchart

During the kneading process, the $FHOR_RS_C$ uploads the horizontal position data of the fingers to the RK3588, which stores the data. After completing the kneading operation for the current layer, the $FVER_DVER_C$ moves the fingers and the sensor upward to perform kneading on the next layer. After each complete kneading operation corresponding to the preset feeding depth, the distance sensor performs a full scan of the kneaded object. Working together with the $FHOR_RS_C$, the system records the rotary stage motor angle and distance sensor data, forming a point cloud dataset. The complete control flow is illustrated in Fig. 4.

2.2. Design of the 3D Model for Kneading Geometry

Five geometric models were designed, including a square prism with a base side length of 53 mm and a height of 40 mm, a cylinder with a diameter of 60 mm and a height of 40 mm, as well as three geometrically complex shapes: the Slim Waist, Helical Truncated Octagonal Frustum, and Concave Cylinder. The geometric parameters of these three complex geometries are provided in Sections 2.2.1, 2.2.2 and 2.2.3. Fig. 5 show the geometries

modeled in SolidWorks and the corresponding physical objects fabricated using a Bambu Lab 3D printer.

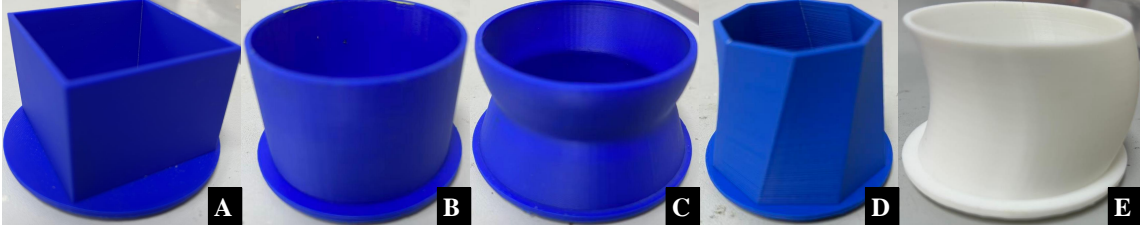


Figure 5: The 3D-printed geometry

2.2.1. Slim waist math equation

Slim waist the curve is generated using the spline curve feature in SolidWorks software, which is a B-spline curve. A two-dimensional cubic B-spline is used. The formula is as follows: let the control points be $P_i = (x_i, y_i)$, $i = 0, \dots, 8$, and the degree be $p = 3$, $P_i = (x_i, y_i)$ and 3D model in Fig .6. Let $C(t)$ denote the point on the spline curve corresponding to the parameter t , where $N_{i,3}(t)$ is the cubic B-spline basis function. The parametric form of the B-spline is Equ.1, Here, $N_{i,3}(t)$ denotes the cubic B-spline basis function, defined recursively by the Cox–de Boor formula. $N_{i,0}(t)$ is the zero-degree basis function is Equ.2, and $N_{i,p}(t)$ represents the B-spline basis function of degree p associated with the i -th control point P_i is Equ.3. In these expressions, t is the curve parameter, i is the control point index, p is the degree of the basis function, and u_i denotes the i -th knot.

$$C(t) = \sum_{i=0}^8 N_{i,3}(t) P_i, \quad t \in [0, 1] \quad (1)$$

$$N_{i,0}(t) = \begin{cases} 1, & \text{if } u_i \leq t < u_{i+1} \\ 0, & \text{otherwise} \end{cases} \quad (2)$$

$$N_{i,p}(t) = \frac{t - u_i}{u_{i+p} - u_i} N_{i,p-1}(t) + \frac{u_{i+p+1} - t}{u_{i+p+1} - u_{i+1}} N_{i+1,p-1}(t) \quad (3)$$

The curve generated by the B-spline is revolved around the Z axis to create the slim-waist surface, where the radius of the surface at each point corresponds to the points on the B-spline curve is Equ.4, the R_i is each control point. Parametric equation of the slim-waist surface is Equ.5.

$$r(z) = \sum_{i=0}^n N_{i,3}(t(z)) R_i, t(z) = \frac{z - z_{\min}}{z_{\max} - z_{\min}} \quad (4)$$

$$X(\theta, z) = (x, y, z) = (r(z) \cos \theta, r(z) \sin \theta, z), \quad \theta \in [0, 2\pi), z \in [0, h] \quad (5)$$

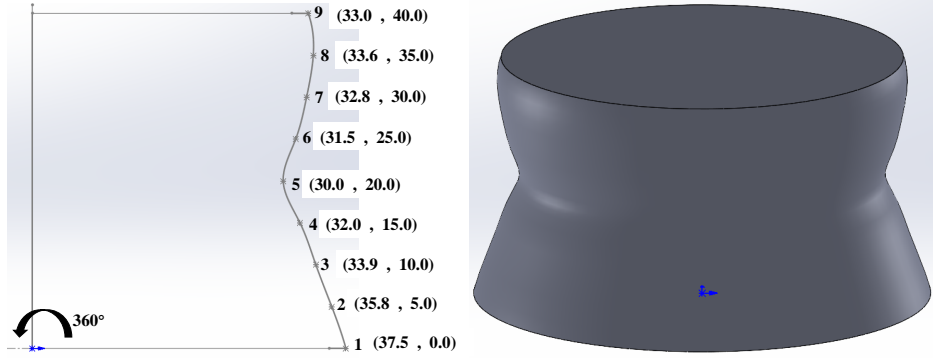


Figure 6: Constraint points and 3D model of the slim waist curve

2.2.2. Helical truncated octagonal frustum math equation

Let the total height be h , the number of layers be N , the inradius of the upper inscribed octagon be r_1 , the inradius of the lower inscribed octagon be r_2 , and the total twist angle be Θ , in Fig .7 (i.e., the rotation of the lower base relative to the upper base) . For the k -th layer, the parameters are defined as follows: the parameter t is a normalized variable (typically mapped along the height direction, either $0 \sim 1$ or $0 \sim N$ layers); $r(t)$ is the radius function that determines the cross-sectional size of the layer and can represent either a linear frustum or a curved variation; $z(t)$ is the height function that gives the coordinate along the Z -axis; $\theta(t)$ is the accumulated twist angle along the height that governs the helical or torsional behavior, is Equ.6. And ϕ_i is the initial angular position of the i -th vertex before twisting, the k layers i nodes is Equ.7

$$\begin{cases} t = \frac{N}{k}, \\ r(t) = r_1 + (r_2 - r_1)t, \\ \theta(t) = \Theta t, z(t) = ht \end{cases} \quad (6)$$

$$\begin{cases} \phi_i = \frac{8\pi}{2}i, \\ P_{k,i} = (r(t) \cos(\phi_i + \theta(t)), r(t) \sin(\phi_i + \theta(t)), z(t)) \end{cases} \quad (7)$$

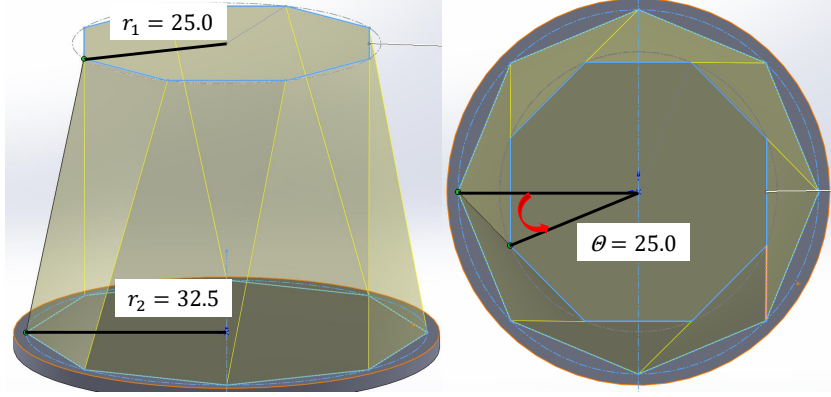


Figure 7: Helical truncated octagonal frustum params and model

2.2.3. Concave cylinder math equation

Concave cylinder use SolidWorks drawing, the surface is generated by lofting through three points: $P_0 = (0, r, 0)$, $P_m = (0, y_0 + r, \frac{h}{2})$, $P_h = (0, r, h)$, in Fig .8. Let the center of the circle be denoted by C , and its trajectory by $C(z)$ is Equ.8, $d(z)$ is Equ.9. The parametric formulation of a concave cylinder is Equ.10

$$C(z) = (0, d(z), z), \quad z \in [0, h] \quad (8)$$

$$d(z) = 4y \cdot \frac{z}{h} \left(1 - \frac{z}{h}\right) \quad (9)$$

$$\mathbf{X}(\theta, z) = (x(\theta, z), y(\theta, z), z) = (r \cos \theta, d(z) + r \sin \theta, z) \quad (10)$$

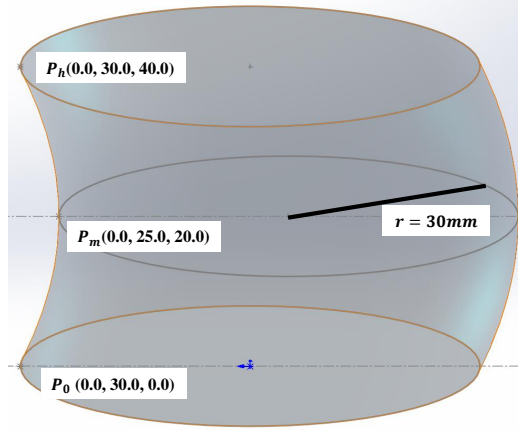


Figure 8: Concave cylinder params and model

3. Geometric Point Cloud Processing for Kneading Generation

3.1. Layer-Based Contour Extraction Algorithm from STL Mesh with Convex Hull

The STL mesh model consists of a large number of triangular facets that describe the surface geometry of a 3D object. To extract cross-sectional contours for subsequent analysis or manufacturing simulation, a layer-based contour extraction algorithm is applied. The algorithm slices the STL model along the vertical Z direction with a fixed layer thickness of $\Delta h = 0.1$ mm. For each slicing plane at height $z = h_i$, the intersection between the plane and the mesh is computed. For a triangular facet with vertices $P_1(x_1, y_1, z_1)$, $P_2(x_2, y_2, z_2)$, $P_3(x_3, y_3, z_3)$, the plane intersects the triangle if satisfies Equ.11.

$$\begin{cases} (z_1 - h_i)(z_2 - h_i) < 0 & \text{or} \\ (z_2 - h_i)(z_3 - h_i) < 0 & \text{or} \\ (z_3 - h_i)(z_1 - h_i) < 0 \end{cases} \quad (11)$$

The intersection points along the edges are obtained by linear interpolation as Equ.12, and similarly for other edges. All intersection points of the current layer form the contour point set $\mathcal{P}_i = \{P_{i1}, P_{i2}, \dots, P_{in}\}$. To obtain a smooth, ordered outer contour, the algorithm applies a **convex hull** operation. Let $\mathcal{P}_i \subset \mathbb{R}^2$ denote the 2D projection of the contour points onto the XY plane. The convex hull is defined as the minimal convex polygon

enclosing all points as Equ.13. Once \mathcal{C}_i is obtained, the perimeter of the contour L_i is calculated as Equ.14, and the contour is resampled uniformly into $N = 400$ points with spacing d as Equ.15. This procedure is repeated for all slicing planes as in Fig .9, $d_1 = d_2 = d_3 = \dots = d_{40}$ (in Figure sampling numbers is 40, use A and D because the cross-sections B, C, and E are all circular), generating a series of evenly spaced, ordered contour layers, which serve as the basis for geometric analysis, surface reconstruction, or toolpath generation in manufacturing processes.

$$\begin{cases} P_{12} = P_1 + \frac{h_i - z_1}{z_2 - z_1}(P_2 - P_1) \\ P_{13} = P_1 + \frac{h_i - z_1}{z_3 - z_1}(P_3 - P_1) \end{cases} \quad (12)$$

$$\mathcal{C}_i = \text{ConvexHull}(\mathcal{P}_i) = \left\{ \sum_{k=1}^m \lambda_k P_k \mid \lambda_k \geq 0, \sum_{k=1}^m \lambda_k = 1 \right\}_{\text{boundary}} \quad (13)$$

$$L_i = \sum_{k=1}^{n-1} \|P_i(k+1) - P_{ik}\| + \|P_{i1} - P_{in}\| \quad (14)$$

$$d = \frac{L_i}{N} \quad (15)$$

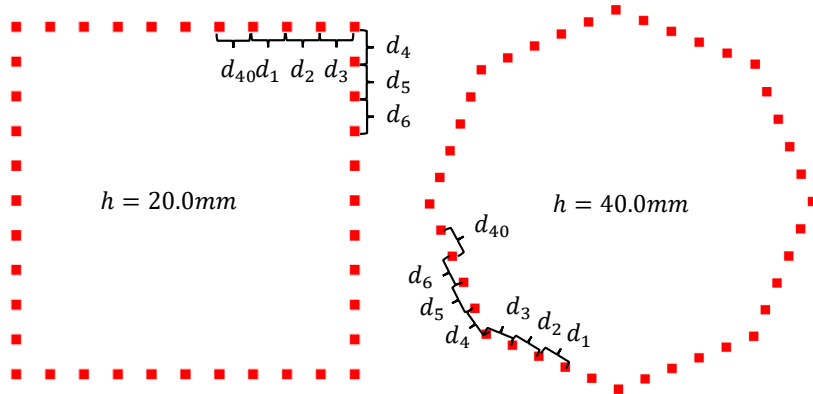


Figure 9: Single layer point cloud sampling

3.2. Determination of Whether a Geometry is an Enveloping Type

According to whether the geometry is of the enveloping type, different kneading methods are applied to geometries such as the cylinder, quadrangular prism, helical truncated octagonal frustum, Slim waist, and concave cylinder. The geometric body is considered an enveloping shape when it simultaneously satisfies the following three criteria: continuity of average radius gradient as Equ.16, monotonicity of cross-sectional area as Equ.17, and regularity of torsion angle as Equ.18. While geometry satisfy $\frac{d\bar{r}}{dz}$, $\frac{dA}{dz}$ and $f(z)$ is continuous, the geometry is considered an enveloping geometry.

$$\bar{r}(z) = \frac{1}{2\pi} \int_0^{2\pi} r(z, \theta) d\theta, \quad \frac{d\bar{r}}{dz} \quad (16)$$

$$A(z) = \int_0^{2\pi} r^2(z, \theta) d\theta, \quad \frac{dA}{dz} \quad (17)$$

$$\frac{d\theta}{dz} = f(z), \quad (18)$$

Table 1: Geometry Classification

Index	Variation of Circumscribed Radius	Section Center Variation	Symmetry Property	Enveloping Shape
A	Constant	Fixed	Axial, Central Symmetry	True
B	Constant	Coaxial	Axial, Central, and Rotational Symmetry	True
C	Continuous variation	Coaxial	Rotational Symmetry	False
D	Linear Variation	Fixed Axis	Rotational Symmetry along Axis	True
E	Constant	Center Translates on Plane along z	Axial Symmetry	False

The circumscribed radius of the sections, section centers, rotational/symmetry properties, and enveloping status of the five geometric bodies are shown in the Tab.1.

3.2.1. Envelope shaping first

The point cloud data are organized into layers according to height, and each layer contains $N_h = 400$ points as Equ.19. Convert the point $(x_{h,i}, y_{h,i})$ into polar coordinates as Equ.20, where $r_{h,i} = D_{h,i}$. A symmetric pairing is established between the left and right fingers as Equ.21, $\{D_{hi}\}_{i=1}^{N'_h} = L_h \cup R_h$. During the kneading process, the turntable rotates over a full circle, while Equ.21 only represents half of the rotation. For the other half, the point cloud data of the left and right fingers are swapped.

$$P = \bigcup_{h=1}^{H_{\max}} P_h, \quad \text{where } P_h = \{(x_{h,i}, y_{h,i}, z_{h,i}) \mid z_{h,i} = h, i = 1, \dots, N_h\}. \quad (19)$$

$$\begin{cases} r_{hi} = \sqrt{x_{hi}^2 + y_{hi}^2} = D_{hi} \\ \theta_{hi} = \text{atan2}(y_{hi}, x_{hi}) \in (-\pi, \pi] \\ z_{hi} = h \end{cases} \quad (20)$$

$$\begin{cases} L_h = \{D_{h1}, \dots, D_{h, \frac{N'_h}{2}}\} \\ R_h = \{D_{h, \frac{N'_h}{2}+1}, \dots, D_{h, N'_h}\} \end{cases} \quad (21)$$

The kneading-forming process is characterized by a layer-by-layer gradual transition. To prevent over-compression or under-forming during shaping, a molding compensation term is introduced into the end-effector displacement as a global correction parameter, as Equ.22, the W is left and right finger in ideal state width. The ideal volume of the molded object is calculated as Equ.23, h_k is the max radius of k layers, The compensated volume is given by Equ.24, $D'(h_k)$ represents the maximum radius of the current k -th layer following the compensation.

$$D_{hi}^{\text{raw}} = \frac{W}{2} - |D_{hi} - s| - m, \quad \text{where } m = \text{mold_scale}. \quad (22)$$

$$V_{\text{orig}} = \sum_{k=1}^n \pi D(h_k)^2 \cdot \Delta h, \quad (23)$$

$$\begin{cases} D'(h_k) = D(h_k) + \Delta r \\ V_{\text{scaled}} = \sum_{k=1}^n \pi D'(h_k)^2 \cdot \Delta h \end{cases} \quad (24)$$

To improve the kneading efficiency, the radius is increased while keeping the volume constant, and the height is recalculated according to the volume ratio. First calculated origin volume and scaled volume ration as Equ.25, H' denotes the height to be kneaded as Equ.26. By calculating the circumference of the point cloud C_h as Equ.27 in the current layer after compensation and dividing it by the diameter of the end-effector d_m , the number of kneading operations required for the current layer is obtained as Equ.28. The kneading step size is then determined based on this number of operations as Equ.28, while m zero is the final forming stage of kneading, the value of K_h is calculated base on $d_m/2$. In the last kneading command is $(h, i, D_{hi}^{\text{raw}}, i + N'_h/2, D_{h, i+N'_h/2}^{\text{raw}})$.

$$\alpha = \frac{V_{\text{orig}}}{V_{\text{scaled}}} \quad (25)$$

$$H' = \{h'_1, h'_2, \dots, h'_n \mid h'_k = h_1 + \alpha(h_k - h_1)\}. \quad (26)$$

$$C_h = 2\pi D'(h_k) \quad (27)$$

$$\begin{cases} K_h = \left\lfloor \frac{C_h}{d_m} \right\rfloor \\ K_h = \left\lfloor \frac{C_h}{d_m/2} \right\rfloor, \quad \text{while } m = 0 \end{cases} \quad (28)$$

$$s_h = \max\left(1, \left\lfloor \frac{N'_h}{K_h} \right\rfloor\right) \quad (29)$$

3.2.2. Similar gradient method

The similar gradient method is a manufacturing approach based on maintaining local consistency of shape across adjacent layers. Its core principle is to achieve global continuity and controllability of deformation through gradual variation between neighboring points or cross-sections. Calculate the cross-sectional area of each layer of the point cloud based on its polar coordinate data as Equ.30, then sum the every layers area as Equ.31, compressed ration calculate as 25. Compressed $H_{\text{max}}^{\text{compressed}}$ calculate as Equ.32, map the points of the compressed layer $H_k^{\text{compressed}}$ to the nearest original layer H^{scaled} .

$$\begin{cases} A_h &= \frac{1}{2} \sum_{i=1}^{n_h} r_i r_{i+1} \sin(\theta_{i+1} - \theta_i), \quad r_1 = r_{n_h+1}, \theta_1 = \theta_{n_h+1} \\ A_h^{\text{scaled}} &= \frac{1}{2} \sum_{i=1}^{n_h} r_i^{\text{new}} r_{i+1}^{\text{new}} \sin(\theta_{i+1} - \theta_i) \end{cases} \quad (30)$$

$$\begin{cases} V_{\text{orig}} = \sum_h A_h \\ V_{\text{scaled}} = \sum_h A_h^{\text{scaled}} \end{cases} \quad (31)$$

$$H_{\text{max}}^{\text{compressed}} = H_{\text{min}} + (H_{\text{max}} - H_{\text{min}}) \cdot \alpha \quad (32)$$

$$H_k^{\text{compressed}} = H_{\text{min}} + k \cdot \Delta H, \quad k = 0, 1, \dots, N-1, \quad H_{N-1}^{\text{compressed}} \leq H_{\text{max}}^{\text{compressed}} \quad (33)$$

$$\begin{cases} \text{idx} = \lfloor \frac{k}{N} \cdot N_{\text{layers}} \rfloor, \quad \text{layer_H}[\text{idx}] = H^{\text{scaled}} \\ \{(H_k^{\text{compressed}}, A_i, D_i^{\text{draw}})\}_{i=1}^{n_{\text{layer}}} \end{cases} \quad (34)$$

3.3. From Point Cloud to Kneading Command: Overview

The proposed kneading instruction generation algorithm first extracts point cloud data from the STL mesh model through layer-based slicing and converts it into a polar coordinate representation for geometric analysis. Based on the continuity of the average radius gradient, the monotonicity of the cross-sectional area, and the regularity of the torsion angle, the geometry is classified as either enveloping or non-enveloping. For enveloping geometries, the Envelope Shaping First method is applied, whereas the Similar Gradient Method is used for non-enveloping geometries.

Subsequently, the kneading path is adaptively generated according to the minimum-radius principle and the geometric characteristics of each layer. The algorithm determines the feed and step parameters based on the end-effector diameter and radial compensation, ensuring a continuous and volume-consistent forming process. The final output consists of an optimized kneading instruction sequence for precise and efficient shaping. Algorithm is summarized in Code 1

Algorithm 1 Adaptive Kneading Data Generation Based on Geometric Features

Require: STL mesh file, end-effector diameter d_m , blank point cloud

Ensure: Kneading command set $Kneading_Commands$

- 1: Read STL file and extract mesh vertices
 - 2: Generate point cloud $P = \{p_i(x_i, y_i, z_i)\}$ and sort by height z
 - 3: **for** each slicing layer h_i **do**
 - 4: Set layer thickness $\Delta h = 0.1$ mm
 - 5: Extract current layer point cloud C_i
 - 6: Convert C_i to polar coordinates (r_i, θ_i)
 - 7: Compute mean radius \bar{r}_i , section area A_i , and torsion function $f(z_i)$
 - 8: **end for**
 - 9: Determine geometry type:
 - 10: **if** $\frac{d\bar{r}}{dz}$, $\frac{dA}{dz}$, and $f(z)$ are continuous **then**
 - 11: Geometry is **enveloping type**
 - 12: **else**
 - 13: Geometry is **non-enveloping type**
 - 14: **end if**
 - 15: Select kneading method:
 - 16: **if** enveloping geometry **then**
 - 17: Apply *Envelope Shaping First* method
 - 18: **else**
 - 19: Apply *Similar Gradient Method*
 - 20: **end if**
 - 21: For each layer, compute perimeter:
 - 22: $L_i = \sum_{k=1}^{n-1} \|P_{i,k+1} - P_{i,k}\| + \|P_{i,1} - P_{i,n}\|$
 - 23: Resample each layer to $N = 400$ points
 - 24: Generate kneading commands based on minimum radius principle:
 - 25: $\Delta r_{\max} = R_{blank}^{\max} - R_{mold}^{\min}$
 - 26: **if** $\Delta r_{\max} \neq 0$ **then**
 - 27: $height_step = d_m - 1$, $radial_step = d_m$
 - 28: **while** $\Delta r_{\max} > 0$ **do**
 - 29: Perform kneading with feed depth = 1 mm
 - 30: $\Delta r_{\max} \leftarrow \Delta r_{\max} - 1$
 - 31: **end while**
 - 32: **else**
 - 33: $height_step = d_m/2$, $radial_step = d_m/2$
 - 34: **end if**
 - 35: Output final kneading commands $Kneading_Commands$
-

4. Experimental and Data Comparative Analysis

4.1. Area of the surface

General ring-mesh method: core concept (continuous to discrete). In the ideal case, the surface area of a smooth surface S is given by Equ.35, where \mathbf{n} is the normal vector of the surface. However, for a point cloud, the surface is discrete and lacks a parametric equation, normal vectors, or an analytical expression.

Therefore, we approximate the surface integral using a triangular mesh of the surface is Equ.36 where A_i is the area of the i -th triangle in the mesh and M is the total number of triangles. According to the point cloud sampling method, where there are 400 points per loop with a vertical spacing of $\Delta z = 1$ mm, the point cloud naturally forms a two-dimensional mesh. Here, \mathbf{v} denotes the vertices used to construct the triangles Equ.37: let k denote the layer index along the height direction, and j denote the angular order of points on each loop, with $M = 400$ points per loop. The points between every two consecutive layers are connected to form quadrilaterals, which are then divided into two triangles as Equ.38. here, mod denotes the modulo operation. Let the vertices of a quadrilateral be denoted as Equ.39. The quadrilateral can then be divided into two triangles, as Equ.40, triangles area calculates as Equ.41. In the last, the total surface area is calculated as Equ.42

$$A = \iint_S \|\mathbf{n}\| dS \quad (35)$$

$$A \approx \sum_{\Delta} \text{Area}(\Delta) \quad (36)$$

$$\mathbf{v}_{k,j} = (x, y, z), \quad k = 0, \dots, K, \quad j = 0, \dots, M - 1 \quad (37)$$

$$j^+ = (j + 1) \bmod M \quad (38)$$

$$Q_{k,j} = [\mathbf{v}_{k,j}, \mathbf{v}_{k+1,j}, \mathbf{v}_{k+1,j^+}, \mathbf{v}_{k,j^+}] \quad (39)$$

$$\Delta = \begin{cases} \Delta_1 = (\mathbf{v}_{k,j}, \mathbf{v}_{k+1,j}, \mathbf{v}_{k+1,j^+}) \\ \Delta_2 = (\mathbf{v}_{k,j}, \mathbf{v}_{k+1,j^+}, \mathbf{v}_{k,j^+}) \end{cases} \quad (40)$$

$$\text{Area}(T) = \frac{1}{2} \|(B - A) \times (C - A)\| \quad (41)$$

$$A_{\text{surface}} \approx \sum_{k=0}^{K-1} \sum_{j=0}^{M-1} \left[\frac{1}{2} \|(\mathbf{v}_{k+1,j} - \mathbf{v}_{k,j}) \times (\mathbf{v}_{k+1,j^+} - \mathbf{v}_{k,j})\| + \frac{1}{2} \|(\mathbf{v}_{k,j^+} - \mathbf{v}_{k,j}) \times (\mathbf{v}_{k+1,j^+} - \mathbf{v}_{k,j})\| \right] \quad (42)$$

4.2. Comparison of Kneaded Point Cloud

Designed three types of end-effectors, as shown in Fig .10. End-effector I ($w_m = 3 \text{ mm}$) pushes the non-kneading surface of the billet when kneading geometries C and E. End-effector II can knead geometries C and E, but after 100,000 kneading cycles, design factors cause burrs to appear on the tool head, which scratch the billet during retraction in Fig .11. End-effector III overcomes the shortcomings of I and II, avoiding contact with the non-kneading surface and preventing material from being drawn out during tool retraction thanks to its frustum-shaped head design.

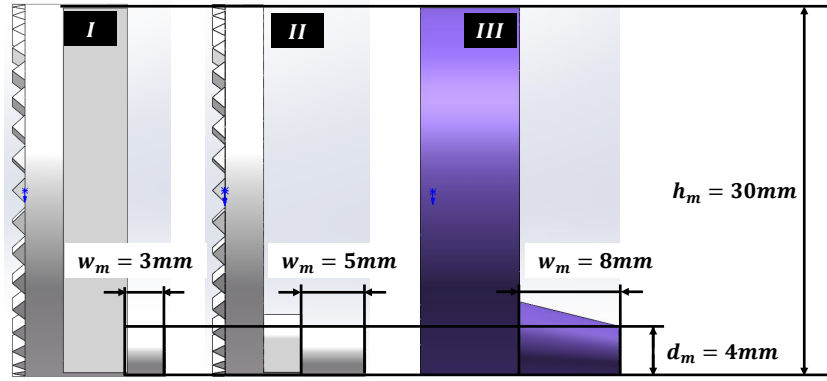


Figure 10: Three versions of End-effector

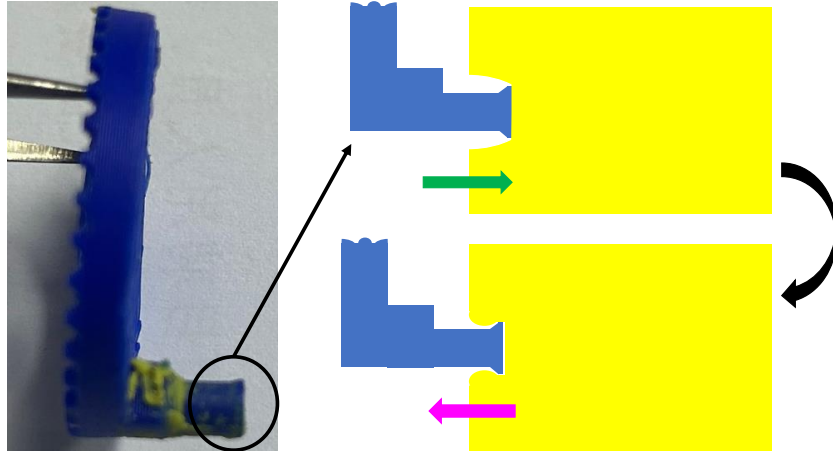


Figure 11: Retraction pulled out material

4.2.1. Ideal Kneading

The end-effector diameter is $d_m = 4mm$. The circular surfaces of two end-effectors are perpendicular to XOY plane and parallel to XOZ plane, moving horizontally toward each other along the Y-axis, as Fig .12.

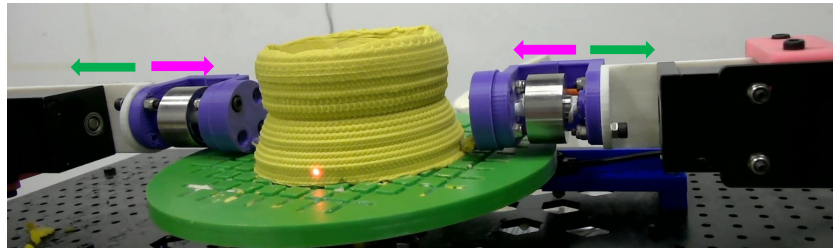


Figure 12: End-effector reciprocating motion

kneading is performed layer by layer, and the actual kneading range for each layer is shown in Fig .13. I shows the kneading range of the end-effector at $layer_i$. After the kneading of $layer_i$ is completed, $layer_{i+1}$ is molded as shown in II. III illustrates the effective point cloud ranges of $layer_i$ and $layer_{i+1}$. When the molding of $layer_{i+1}$ is completed, only the lower half of the end-effector's molding range in $layer_i$ remains effective (since the molding is performed layer by layer from bottom to top, only the lower half is active).

Therefore, according to the situation shown in Fig. 250 and based on the molding commands generated in Sec 3.2.1 and Sec 3.2.2, the kneading

command is used to construct the ideal machining PCL mapped onto the end-effector.

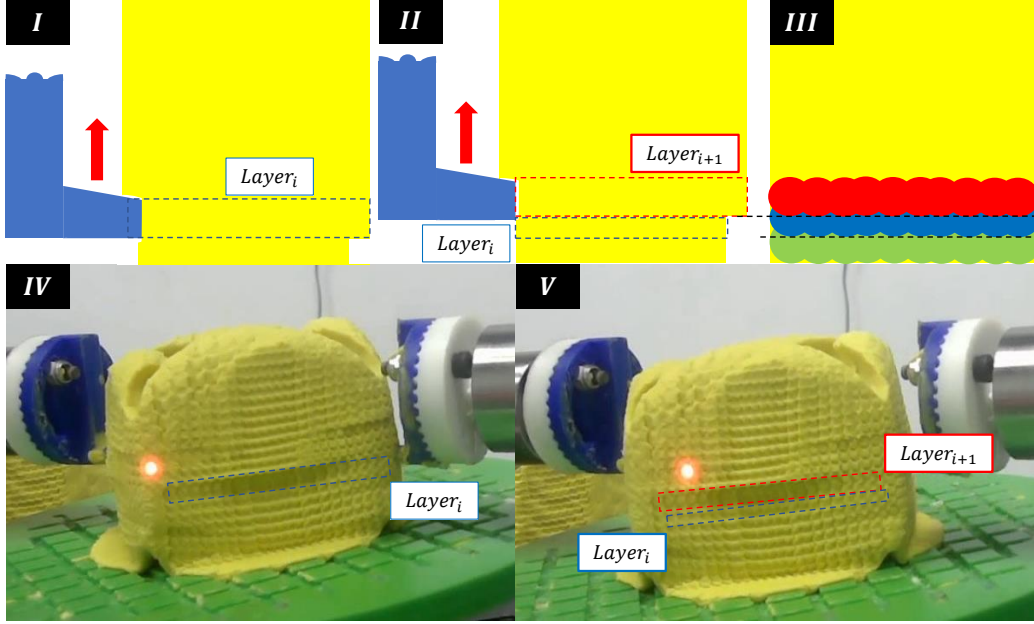


Figure 13: Actual Knead range

The commands $(h, i, D_{hi}^{\text{raw}}, i + N'_h/2, D_{h, i+N'_h/2}^{\text{raw}})$ are inversely used to generate a point cloud. Then, for each point in the cloud, a semicircular point cloud representing the actual effective area of the end-effector is generated, with each semicircle centered at the corresponding point, perpendicular to XOY plane. Get one point from point cloud, is the circle center c_i , the normal vector \mathbf{n}_i of the circular surface is the unit vector from the circle center pointing toward the Z-axis, let \mathbf{u}_i and \mathbf{v}_i be two unit vectors lying in the plane, perpendicular to each other and perpendicular to the normal vector, because the circle plane perpendicular to XOY plane, so can use the \mathbf{u}_i is $(0, 0, 1)$, as Equ.43. Then assume generates N_{gp} points within the circular area of diameter d_m end-effector, each generated circular ring is r_{gpi} , as Equ.44. The number of points on each circular ring varies with the radius (to ensure approximately uniform point density along the ring) as Equ.45, K represents the minimum number of points on each circular ring, to avoid shape distortion caused by overly sparse sampling near the center of the ring, K is typically set to 8, 12, or 16. Points on each ring are evenly distributed in

angle as Equ.46. In the end the uniformly distributed point cloud coordinates $\mathbf{p}_{k,j}$ generated with c_i as the circle center are show in Equ.47.

$$\mathbf{v}_i = \frac{\mathbf{n}_i \times \mathbf{u}_i}{\|\mathbf{n}_i \times \mathbf{u}_i\|} \quad (43)$$

$$r_{\text{gpi}} = \frac{d_m * k}{2 * \text{int}(\sqrt{N_{gp}})}, \quad k = 1, 2, \dots, \sqrt{N_{gp}} \quad (44)$$

$$n_{\text{points},k} = \max \left(K, \text{int} \left(\frac{2\pi r_k}{R/(\sqrt{N_{gp}})} \right) \right) \quad (45)$$

$$\theta_j = \frac{2\pi j}{n_{\text{points},k}}, \quad j = 0, 1, \dots, n_{\text{points},k} - 1 \quad (46)$$

$$\mathbf{p}_{k,j} = \mathbf{c}_i + r_k \cos(\theta_j)\mathbf{u}_i + r_k \sin(\theta_j)\mathbf{v}_i \quad (47)$$

According to Equ.47, the generated ideal machining PCL(set $N_{gp} = 40$) is shown in Fig .14. A, B, and D are placed in the first layer because they are processed using the enveloping method, C and E are placed in the second layer because they are processed using the similarity method.

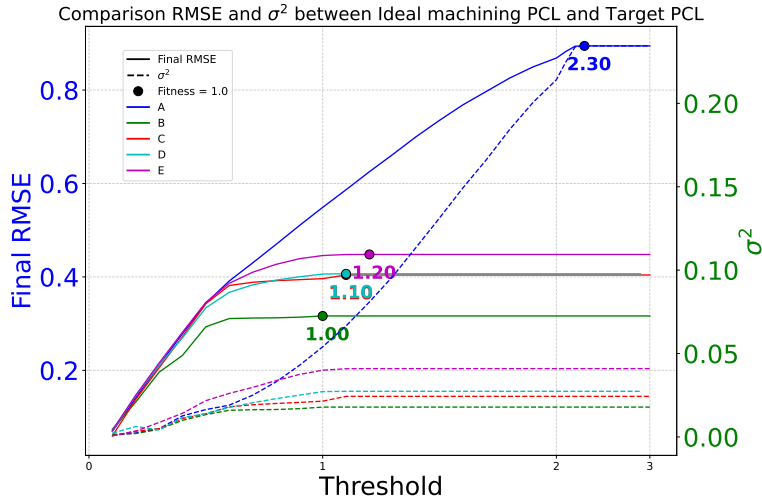


Figure 15: Comparison RMSE and σ^2 between Ideal machining PCL and Target PCL

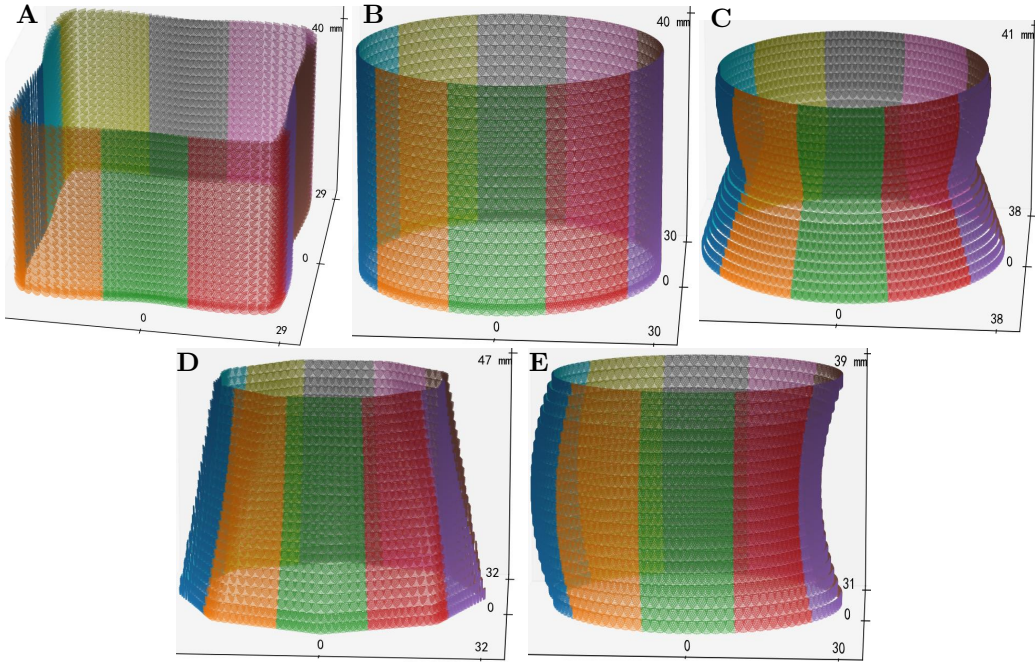


Figure 14: Ideal machining point cloud

The ideal machining PCL and the target PCL extracted from the STL model were registered using the ICP algorithm. By adjusting the distance threshold, the fitness was optimized to 1.0. The ideal machining accuracy was evaluated using the obtained root mean square error (RMSE) and residual variance (σ^2). The variations of ICP registration results with distance threshold for the five geometries A, B, C, D, and E are shown in Fig. 15. Final registration results of the five geometric objects are shown in the Tab. 2.

Table 2: Ideal machining PCL and Target PCL ICP registration results

Geometric	Threshold	RMSE
A	2.3	0.895
B	1	0.316
C	1.1	0.404
D	1.1	0.407
E	1.2	0.448

4.2.2. Actual Kneading result

To evaluate the geometric fidelity of the kneading-based forming process, the actual kneading point clouds (Actual Kneading PCLs) of Geometries A–E are systematically compared with the corresponding 3D-printed reference point clouds (Target PCLs), as well as with the compensated point clouds obtained through RMSE-based correction. The kneading-based forming processes of Geometries A, B, C, D, and E are illustrated in Fig. 16. Geometry A demonstrates the transformation of a circular blank with an initial diameter of 80 mm into a square prism, while Fig. 16-B shows the forming process from a square-based blank with a diagonal length of 84.5 mm into a cylindrical geometry. Fig. 16-C, D, and E present the kneading processes of the corresponding geometries using the Similar Gradient method. These results visually confirm that the proposed kneading platform can realize both envelope-type and non-envelope-type geometries through adaptive kneading strategies.

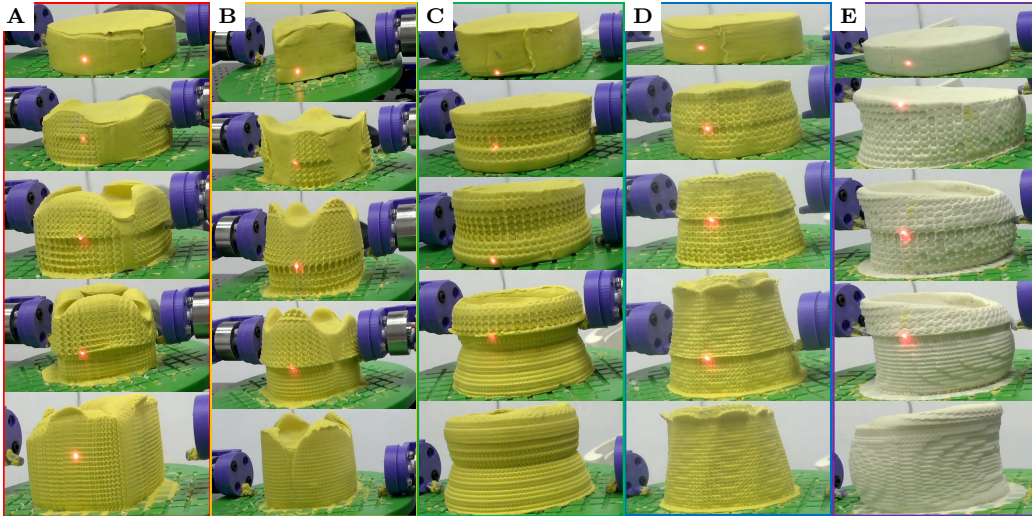


Figure 16: Geometric actual knead result

During the forming process, the evolution of the blank surface area is shown in Fig. 17. For all five geometries, the final formed blanks exhibit surface areas and heights larger than the corresponding ideal values. This deviation is mainly attributed to two factors, as illustrated in Fig. 18: (i) material flow on the blank surface during kneading, which induces cavities in the upper regions of the formed geometries, and (ii) elastic rebound of the

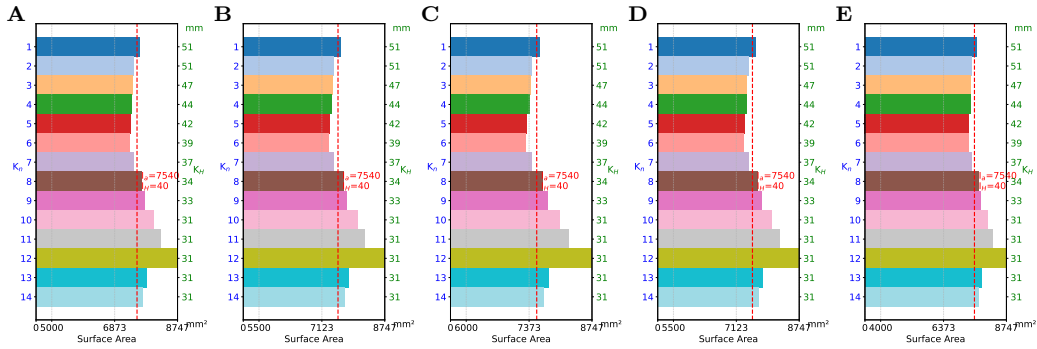


Figure 17: Geometric Knead area of surface

material after the completion of kneading. These effects jointly introduce systematic geometric deviations in the actual kneading results.

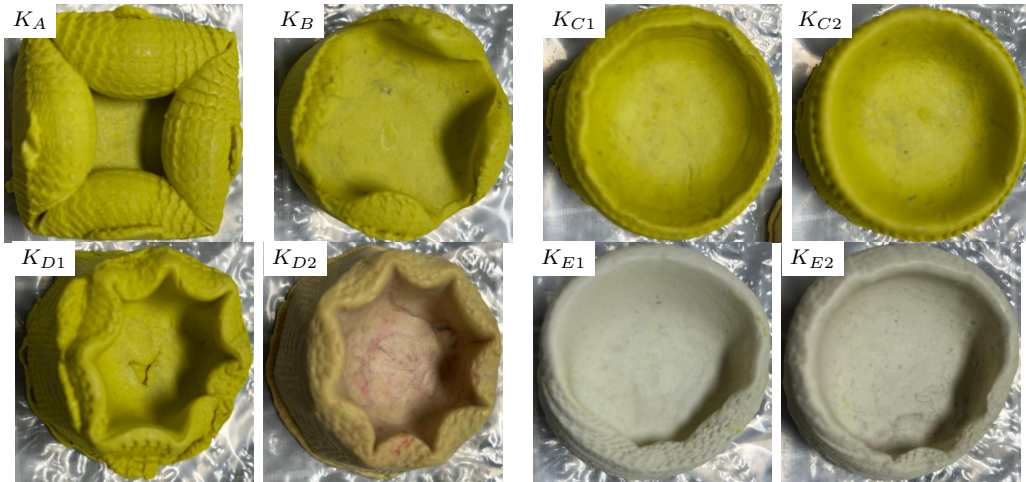


Figure 18: Geometric model top is hollowed

Material utilization during the kneading process is quantified by comparing the material mass before and after forming, as shown in Fig. 19. For Geometries A and B, as well as Geometries C, D, and E formed using two different kneading strategies, the material utilization consistently exceeds 98%. The primary sources of material loss are illustrated in Fig. 20, including adhesion between the fingers and the material and material detachment caused by the grooved structure of the rotating frustum platform. A comparative summary of material utilization for conventional subtractive manufacturing, additive manufacturing, and the proposed kneading-based forming method

is provided in Tab. 3, highlighting the material efficiency advantage of the proposed approach.

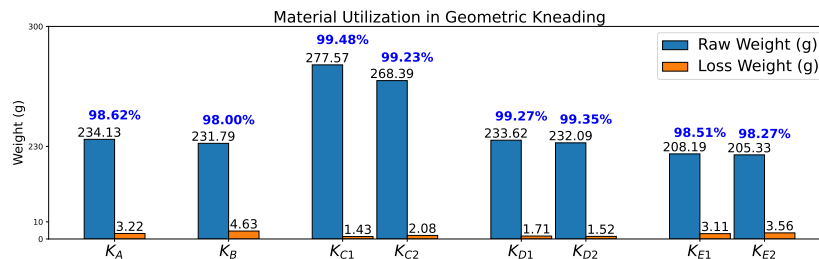


Figure 19: Geometric material mass change before and after kneading

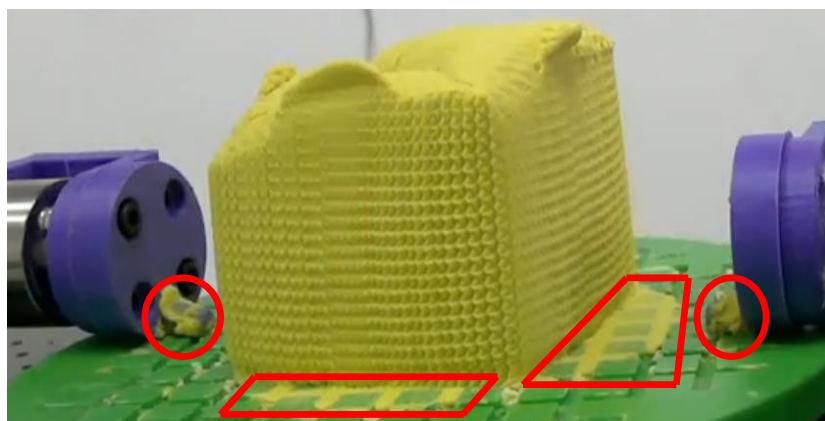


Figure 20: Material loss in the kneading process

Table 3: Material utilization efficiency of different manufacturing methods

Process	Utilization (%)	Scrap Type	Recyclability
SM	~30–60	Chips	Medium
AM	~70–90	Support waste	Low–Medium
Our	≥98	None	High

The processing time and the number of kneading cycles for each geometry are presented in Fig. 21. The required number of processing cycles is primarily determined by the dimensional difference between the initial blank

and the target geometry. Geometry A exhibits the largest dimensional difference and therefore requires the greatest number of kneading cycles, resulting in the longest processing time. For Geometry C, the kneading times of the two methods are nearly identical. In contrast, for Geometry D, the Similar Gradient method requires approximately one additional hour compared to the Envelope Shaping First method, whereas for Geometry E, the Envelope Shaping First method requires approximately two additional hours. These results indicate that, under identical initial blank dimensions and processing cycle counts, the intrinsic geometric characteristics of the object dominate the overall processing time.

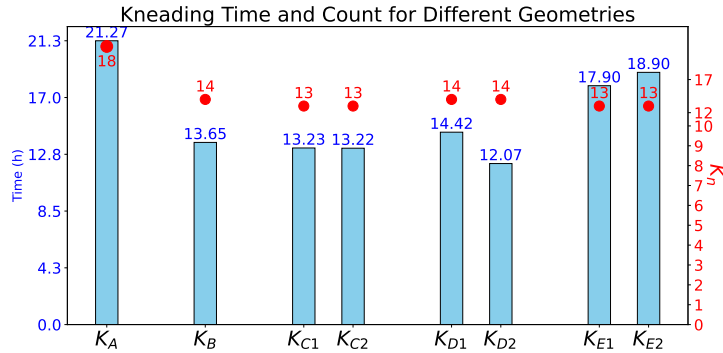


Figure 21: Geometric knead time and knead cycles

As shown in Fig. 15 and Tab. 2, the Threshold values at which the fitness reaches 1.0 are close for Geometries B, C, D, and E, while Geometry A exhibits the largest Threshold at the same fitness level. This difference is primarily related to cross-sectional geometry: B, C, and E have circular cross-sections, D has an octagonal cross-section approximating a circle, whereas A has a square cross-section that deviates most from circularity, leading to reduced ideal machining accuracy.

After each kneading operation with the preset cutting depth from bottom to top, the entire blank is scanned. The actual machining accuracy is evaluated by performing ICP registration between the point cloud obtained from the final molded blank scan and the target PCL. The machining accuracy is quantified using the RMSE and σ^2 obtained from the ICP registration. For consistency, the actual kneading PCLs used for comparison are extracted at the same height as the corresponding target PCLs.

For Geometries A and B, the kneading process involves a discrete transformation of the cross-sectional shape between the initial blank and the target geometry. Specifically, Geometry A is formed from a cylindrical blank with a circular cross-section into a square prism, whereas Geometry B is formed from a square-based blank into a cylindrical geometry. Such non-continuous geometric transitions introduce additional deformation complexity compared to geometries with continuous cross-sectional evolution.

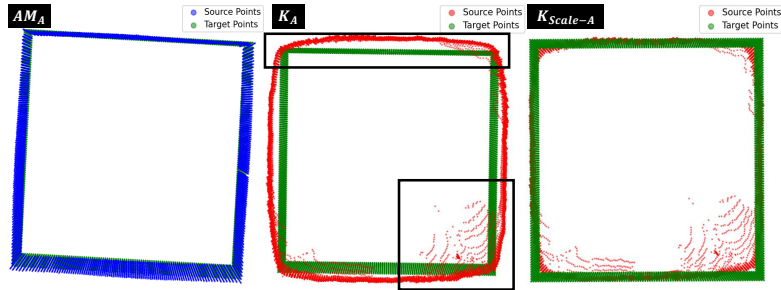


Figure 22: Geometric A: Registration results between Actual knead, Compensate PCL and Target PCL

As shown in Fig. 22, Geometry A exhibits a pronounced global scale expansion after kneading. The deviation between the actual kneaded PCL and the target PCL is spatially uniform and extends across both the side-walls and top region. This behavior indicates that the dominant error source in Geometry A is elastic rebound of the material after the completion of kneading. Moreover, due to the transformation from a circular to a square cross-section, stress redistribution is amplified in the corner regions, leading to larger RMSE and more irregular variations in σ^2 compared with other geometries. After applying RMSE-based compensation, the compensated PCL shows a significantly improved overlap with the target PCL.

The quantitative ICP registration results for Geometry A are shown in Fig. 23. Before compensation, the actual kneaded PCL requires a relatively large Threshold to reach a fitness of 1.0, and the corresponding σ^2 exhibits irregular fluctuations as the Threshold increases. After compensation, the RMSE variation curve becomes smoother and approaches that of the ideal kneading result, while σ^2 converges more steadily. The significance analysis further confirms that the differences between the 3D-printed reference PCL and the actual kneading PCL are statistically significant in both RMSE and σ^2 .

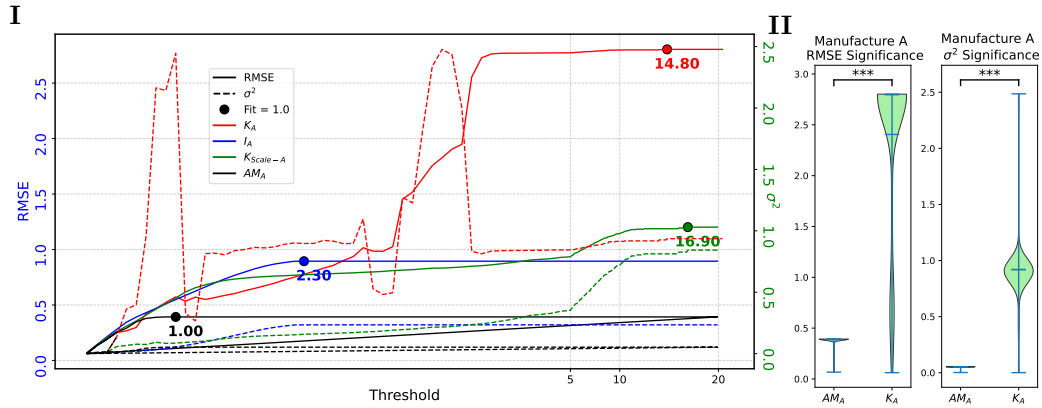


Figure 23: Geometric A: I: Comparison RMSE and σ^2 of Actual, Ideal Kneading, AM and Target PCL; II: RMSE and σ^2 Significance Analysis

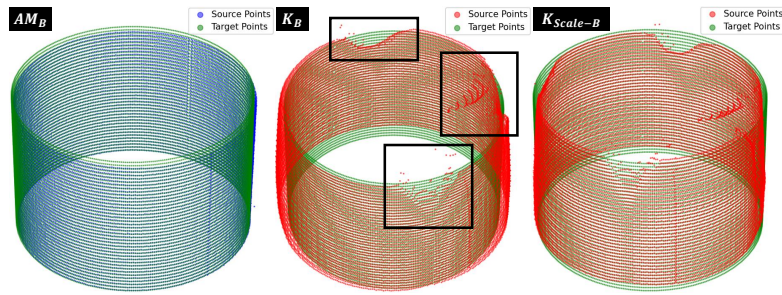


Figure 24: Geometric B: Registration results between Actual knead, Compensate PCL and Target PCL

In contrast, Geometry B demonstrates a different error pattern. As illustrated in Fig. 24, although the overall cylindrical shape is successfully formed, local corner-related defects are observed in the actual kneaded PCL. These defects, highlighted by the black boxes, originate from the initial square blank, where insufficient material redistribution at the corner regions leads to partial contour loss during the transition to a circular geometry. Such local defects persist even after compensation, although the global geometric consistency of the PCL is improved.

The corresponding ICP results in Fig. 25 show that Geometry B reaches a fitness of 1.0 only at relatively large Threshold values before compensation. This behavior is mainly attributed to the incomplete PCL caused by corner defects, which hinders ICP convergence at smaller Thresholds. After compensation, the RMSE is reduced and the RMSE curve becomes smoother;

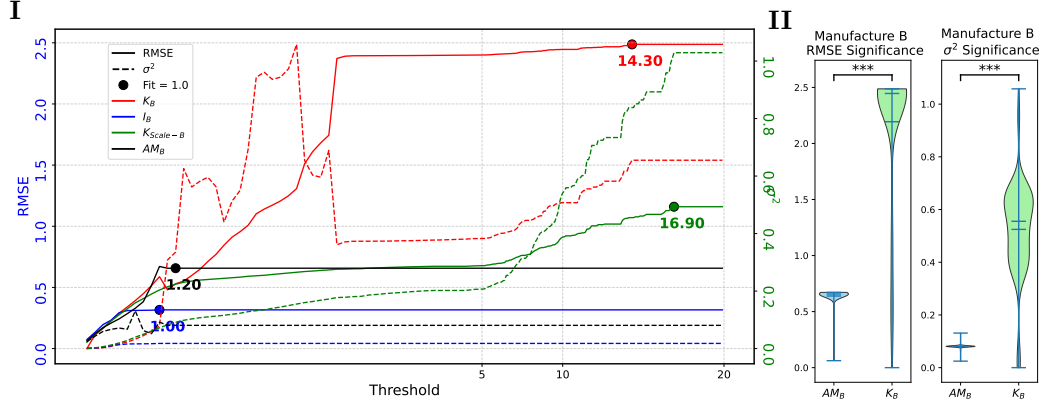


Figure 25: Geometric B: I: Comparison RMSE and σ^2 of Actual, Ideal Kneading, AM and Target PCL; II: RMSE and σ^2 Significance Analysis

however, the residual RMSE remains larger than that of Geometry A. Notably, Geometry B exhibits a smaller σ^2 than Geometry A, indicating that apart from the localized corner defects, the remaining PCL is highly consistent with the target geometry. The significance analysis further verifies that the RMSE and σ^2 differences between the kneaded PCLs and the reference PCL are statistically significant.

Geometries C, D, and E represent geometries with continuous or quasi-continuous axial characteristics and were formed using two kneading strategies: the Similar Gradient method and the Envelope Shaping First method. The corresponding actual kneaded PCLs, compensated PCLs, and target PCLs are shown in Fig. 26, Fig. 28, and Fig. 30, respectively.

For Geometry C, the deviation between the actual kneaded PCL and the target PCL exhibits a gradual axial variation rather than a uniform scale expansion. As shown in Fig. 26, the Similar Gradient method yields a PCL that more closely follows the axial geometric evolution of the target shape, whereas the Envelope Shaping First method shows larger local deviations. After RMSE-based compensation, both methods achieve improved geometric alignment; however, the compensated PCL obtained using the Similar Gradient method exhibits lower RMSE and faster convergence of σ^2 .

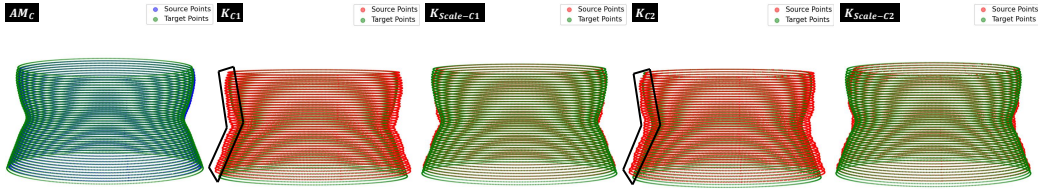


Figure 26: Geometric C: Registration results between Actual knead, Compensate PCL and Target PCL

This trend is quantitatively confirmed by the ICP results in Fig. 27. Before compensation, the Similar Gradient method reaches a fitness of 1.0 at a smaller Threshold than the Envelope Shaping First method. After compensation, this difference becomes more pronounced, with the compensated Similar Gradient PCL approaching the ideal kneading accuracy. The corresponding significance analysis indicates that the differences in RMSE between the two methods are statistically significant, while the differences in σ^2 are less pronounced, suggesting that the primary distinction lies in systematic geometric deviation rather than random dispersion.

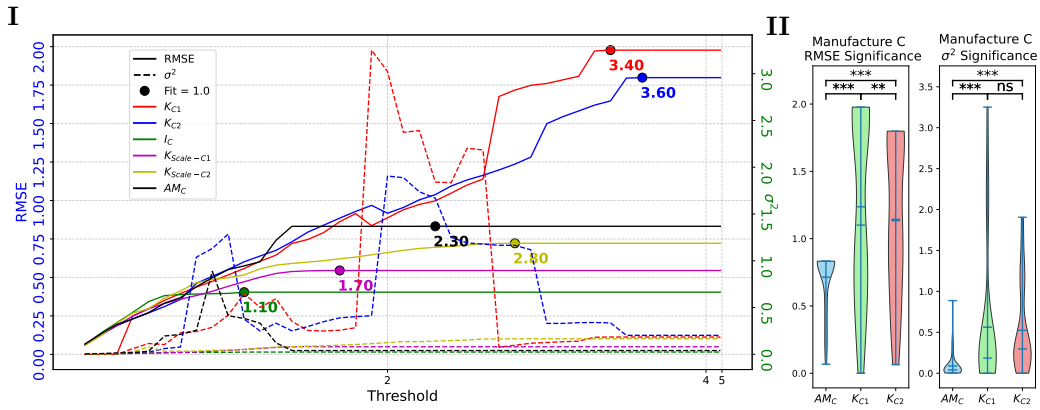


Figure 27: Geometric C: I: Comparison RMSE and σ^2 of Actual, Ideal Kneading, AM and Target PCL; II: RMSE and σ^2 Significance Analysis

Geometry D exhibits behavior dominated by global elastic rebound, similar to Geometry A, but without discrete cross-sectional transformation. As shown in Fig. 28, both kneading methods result in an overall scale expansion of the PCL relative to the target PCL. The black-box regions indicate that the deviation is spatially uniform rather than localized. After compensation, both methods show a substantial improvement in overlap between the

compensated PCLs and the target PCL.

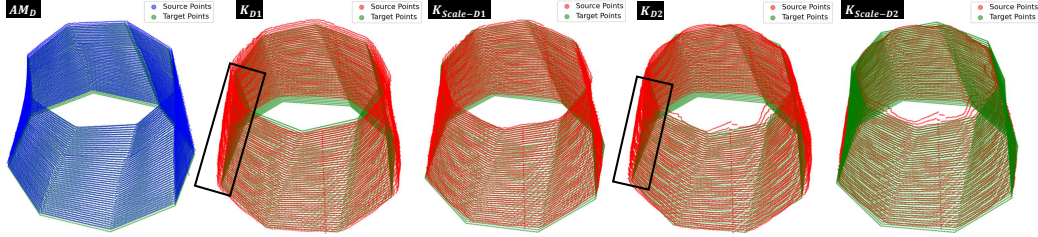


Figure 28: Geometric D: Registration results between Actual knead, Compensate PCL and Target PCL

The ICP results in Fig. 29 reveal that compensation leads to smoother RMSE variation curves and reduced σ^2 values for both methods. Compared with Geometry C, Geometry D requires larger Threshold values to reach a fitness of 1.0, reflecting its larger overall geometric deviation. The significance analysis confirms that both kneading methods differ significantly from the 3D-printed reference PCL in terms of RMSE and σ^2 , while the difference between the two methods is mainly reflected in the stability of the error distribution.

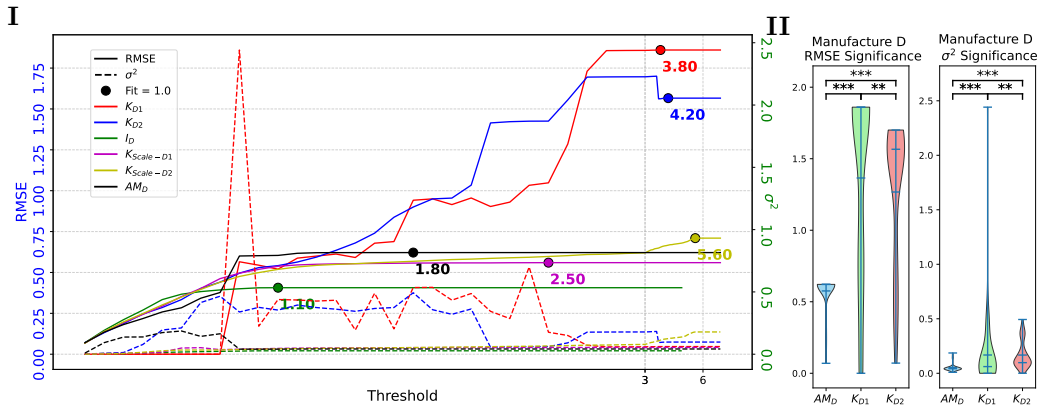


Figure 29: Geometric D: I: Comparison RMSE and σ^2 of Actual, Ideal Kneading, AM and Target PCL; II: RMSE and σ^2 Significance Analysis

Geometry E exhibits a distinctly different error mechanism compared with Geometries C and D. As shown in Fig. 30, the primary deviation is not global scale expansion but axial center offset of identical cross-sections in the PCL. Despite having identical cross-sectional shapes and dimensions along

the axis, the centers of these cross-sections deviate systematically, leading to local misalignment that cannot be eliminated through global compensation.

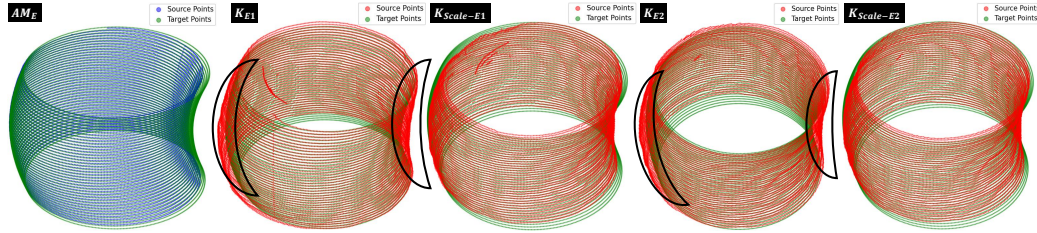


Figure 30: Geometric E: Registration results between Actual knead, Compensate PCL and Target PCL

This behavior is further illustrated in Fig. 31. Before compensation, the RMSE curves of both kneading methods remain relatively stable, while σ^2 exhibits large fluctuations at small Threshold values. After compensation, the Threshold values corresponding to a fitness of 1.0 remain nearly unchanged, indicating that RMSE-based global compensation has limited effectiveness for Geometry E. The significance analysis confirms that both kneading methods differ significantly from the reference PCL, and that the dominant error source is related to kneading command planning rather than material rebound.

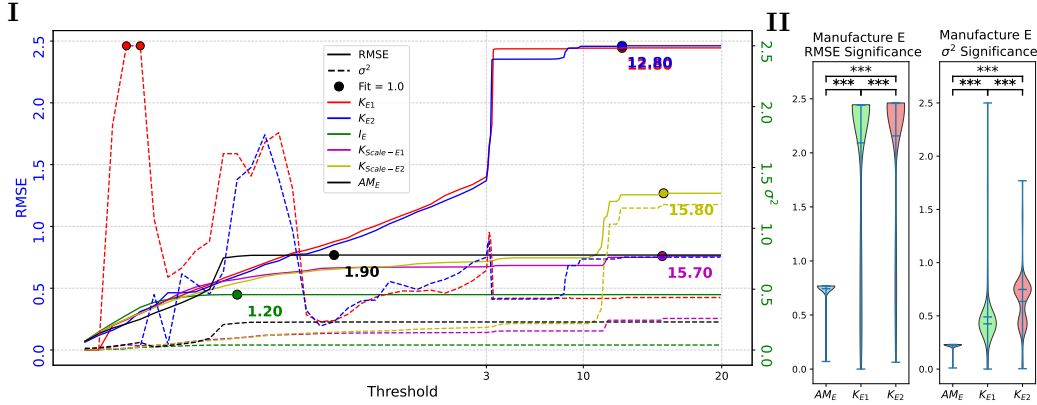


Figure 31: Geometric E: I: Comparison RMSE and σ^2 of Actual, Ideal Kneading, AM and Target PCL; II: RMSE and σ^2 Significance Analysis

Table 4: Geometry ICP Registration between Actual Kneading and Compensated PCL Data

Geometric	Kneading Method	Threshold	RMSE	σ^2
A	K_A	14.8	2.802	0.937
	I_A	2.3	0.895	0.234
	$K_{Scale-A}$	16.9	1.202	0.843
B	K_B	14.3	2.487	0.655
	I_B	1	0.316	0.018
	$K_{Scale-B}$	16.9	1.16	1.029
C	K_{C1}	3.4	1.977	0.185
	K_{C2}	3.6	1.799	0.203
	I_C	1.1	0.404	0.024
	$K_{Scale-C1}$	1.7	0.545	0.081
	$K_{Scale-C2}$	2.8	0.722	0.165
D	K_{D1}	3.8	1.86	0.061
	K_{D2}	4.2	1.567	0.097
	I_D	1.1	0.407	0.027
	$K_{Scale-D1}$	2.5	0.56	0.054
	$K_{Scale-D2}$	5.6	0.71	0.179
E	K_{E1}	12.8	2.445	0.431
	K_{E2}	12.8	2.462	0.763
	I_E	1.2	0.448	0.041
	$K_{Scale-E1}$	15.8	0.76	0.259
	$K_{Scale-E2}$	15.7	1.268	1.195

The overall kneading accuracy of Geometries A–E is quantitatively summarized in Tab. 4. The results reveal that the dominant forming error and the effectiveness of RMSE-based compensation are strongly dependent on the geometric characteristics of the target shape. Geometry A, involving a discrete cross-sectional transformation from circular to square, exhibits the largest RMSE and unstable σ^2 due to amplified elastic rebound and corner-induced stress redistribution, while compensation effectively suppresses this global deviation. Geometry B, formed from a square blank into a circular geometry, is primarily limited by local corner-related material deficiency rather than global scale expansion, leading to reduced RMSE after compensation but persistent residual error. For Geometry C, characterized by continuous axial geometric variation, compensation significantly improves accuracy, with

the Similar Gradient method achieving lower RMSE and faster σ^2 convergence than the Envelope Shaping First method. Geometry D is dominated by uniform elastic rebound, and compensation consistently reduces RMSE for both kneading strategies. In contrast, Geometry E shows limited sensitivity to global compensation, as its dominant error originates from axial center offset rather than material rebound. Overall, RMSE at fitness 1.0 serves as an effective indicator of rebound-dominated error, while the compensated RMSE represents the upper bound of achievable kneading accuracy under given material and environmental conditions.

5. Conclusion

This study proposes a volume-consistent kneading-based forming paradigm for plastic materials, integrating a custom-designed kneading platform, geometry-aware kneading command generation, and PCL-based geometric evaluation. By combining envelope-type and non-envelope-type kneading strategies with layer-wise scanning and ICP-based registration, the proposed system enables continuous shaping of complex three-dimensional geometries with high material utilization.

Experimental validation was conducted on five representative geometries (A–E) covering discrete cross-sectional transformations, continuous axial variations, and center-offset configurations. The results demonstrate that elastic rebound is the dominant source of global geometric deviation for most geometries, and that RMSE at a fitness of 1.0 provides an effective quantitative indicator of rebound-dominated error. RMSE-based compensation significantly improves the geometric fidelity of rebound-dominated geometries, and the compensated RMSE can be regarded as the upper bound of achievable kneading accuracy under given material and environmental conditions.

The comparative analysis further reveals clear geometry-dependent error mechanisms. Geometries involving discrete cross-sectional transformations (A and B) are strongly influenced by corner-induced stress redistribution and material deficiency, while geometries with continuous axial variation (C and D) benefit more consistently from compensation, particularly when combined with the Similar Gradient method. In contrast, Geometry E exhibits limited sensitivity to global compensation due to axial center offset, indicating that its dominant error originates from kneading command planning rather than material rebound.

Overall, the proposed kneading-based forming framework demonstrates high material efficiency (above 98%), controllable geometric accuracy, and strong adaptability to different geometric characteristics. These results highlight the potential of kneading-based forming as a sustainable alternative to conventional additive and subtractive manufacturing for customizable and low-waste fabrication. Future work will focus on adaptive path re-planning and local compensation strategies to address center-offset and non-rebound-dominated geometries.

Appendix A. Example Appendix Section

Appendix text.

References

- [1] C. Li, K. Bhatta, M. Waseem, Q. Chang, Demand-driven hierarchical integrated planning-scheduling control for a mobile robot-operated flexible smart manufacturing system, *Robotics and Computer-Integrated Manufacturing* 95 (2025) 103015.
- [2] D. Mourtzis, M. Doukas, The evolution of manufacturing systems: From craftsmanship to the era of customisation, in: *Handbook of research on design and management of lean production systems*, IGI Global Scientific Publishing, 2014, pp. 1–29.
- [3] V. Le, M. Tran, S. Ding, Subtractive manufacturing of composite materials with robotic manipulators: a comprehensive review, *The International Journal of Advanced Manufacturing Technology* 135 (1) (2024) 81–117.
- [4] G. Ingarao, P. C. Priarone, F. Gagliardi, R. Di Lorenzo, L. Settineri, Subtractive versus mass conserving metal shaping technologies: An environmental impact comparison, *Journal of Cleaner Production* 87 (2015) 862–873.
- [5] L. Proud, D. Whitehead, T. Slatter, P. Crawforth, D. Curtis, Subtractive manufacturing of hazardous materials: A review, *Safety* 11 (4) (2025) 112.

- [6] S. Rescsanski, R. Hebert, A. Haghghi, J. Tang, F. Imani, Towards intelligent cooperative robotics in additive manufacturing: Past, present, and future, *Robotics and Computer-Integrated Manufacturing* 93 (2025) 102925.
- [7] L. Zhou, J. Miller, J. Vezza, M. Mayster, M. Raffay, Q. Justice, Z. Al Tamimi, G. Hansotte, L. D. Sunkara, J. Bernat, Additive manufacturing: a comprehensive review, *Sensors* 24 (9) (2024) 2668.
- [8] P. Tang, X. Zhao, H. Shi, B. Hu, J. Ding, B. Yang, W. Xu, A review of multi-axis additive manufacturing: Potential, opportunity and challenge, *Additive Manufacturing* 83 (2024) 104075.
- [9] A. P. Golhin, R. Tonello, J. R. Frisvad, S. Grammatikos, A. Strandlie, Surface roughness of as-printed polymers: A comprehensive review, *The International Journal of Advanced Manufacturing Technology* 127 (3) (2023) 987–1043.
- [10] J. Jiang, X. Xu, J. Stringer, Support structures for additive manufacturing: a review, *Journal of Manufacturing and Materials Processing* 2 (4) (2018) 64.
- [11] T. A. Yeshiwas, A. B. Tiruneh, M. A. Sisay, A review article on the assessment of additive manufacturing, *Journal of Materials Science: Materials in Engineering* 20 (1) (2025) 85.
- [12] W. Wang, F. van Keulen, J. Wu, Fabrication sequence optimization for minimizing distortion in multi-axis additive manufacturing, *Computer Methods in Applied Mechanics and Engineering* 406 (2023) 115899.
- [13] Y. Lu, et al., Digital Twin-driven smart manufacturing: connotation, reference model, applications and research issues, *Robotics and Computer-Integrated Manufacturing* 61 (2020) 101837.
- [14] H. Kagermann, W. Wahlster, Ten years of Industrie 4.0, *Sci* 4 (3) (2022) 26.
- [15] M. Hankel, B. Rexroth, The reference architectural model Industrie 4.0 (RAMI 4.0), *Zvei* 2 (2) (2015) 4–9.

- [16] A. Trattner, L. Hvam, C. Forza, Z. N. L. Herbert-Hansen, Product complexity and operational performance: A systematic literature review, *CIRP Journal of Manufacturing Science and Technology* 25 (2019) 69–83.
- [17] L. Zhang, X. Chen, W. Zhou, T. Cheng, L. Chen, Z. Guo, B. Han, L. Lu, Digital twins for additive manufacturing: a state-of-the-art review, *Applied Sciences* 10 (23) (2020) 8350.
- [18] C. Martínez-Olvera, Towards the development of a digital twin for a sustainable mass customization 4.0 environment: a literature review of relevant concepts, *Automation* 3 (1) (2022) 197–222.
- [19] D. Braun, T. Müller, N. Sahlab, N. Jazdi, W. Schlögl, M. Weyrich, A graph-based knowledge representation and pattern mining supporting the digital twin creation of existing manufacturing systems, in: *2022 IEEE 27th International Conference on Emerging Technologies and Factory Automation (ETFFA)*, IEEE, 2022, pp. 1–4.
- [20] H. Ni, T. Hu, J. Deng, B. Chen, S. Luo, S. Ji, Digital twin-driven virtual commissioning for robotic machining enhanced by machine learning, *Robotics and Computer-Integrated Manufacturing* 93 (2025) 102908.
- [21] K. Nagayama, J. Yan, Deterministic error compensation for slow tool servo-driven diamond turning of freeform surface with nanometric form accuracy, *Journal of Manufacturing Processes* 64 (2021) 45–57.
- [22] B. Iñigo, N. Colinas-Armijo, L. N. López de Lacalle, G. Aguirre, Digital twin for volumetric thermal error compensation of large machine tools, *Sensors* 24 (19) (2024) 6196.
- [23] E. Rodriguez, A. Alvares, C. Riano, STEP-NC in additive manufacturing: a comprehensive review, architecture, and data model proposal, *The International Journal of Advanced Manufacturing Technology* (2025) 1–37.
- [24] S. T. Newman, Z. Zhu, V. Dhokia, A. Shokrani, Process planning for additive and subtractive manufacturing technologies, *CIRP annals* 64 (1) (2015) 467–470.

- [25] B. Freitas, V. Richhariya, M. Silva, A. Vaz, S. F. Lopes, Ó. Carvalho, A review of hybrid manufacturing: integrating subtractive and additive manufacturing, *Materials* 18 (18) (2025) 4249.
- [26] Ö. B. Çapunaman, A. Mohseni, D. Dombrovskij, K. Yin, B. Gürsoy, M. D. Mylo, A robotic framework for high-throughput and multi-view 3d digital image correlation (3d-dic): Increasing measurement volume and versatility for deformation analysis, *Robotics and Computer-Integrated Manufacturing* 99 (2026) 103187.
- [27] J. Lario, J. Mateos, F. Psarommatis, Á. Ortiz, Towards zero defect and zero waste manufacturing by implementing non-destructive inspection technologies, *Journal of Manufacturing and Materials Processing* 9 (2) (2025) 29.
- [28] M. Javaid, A. Haleem, et al., Studies on the metrological need and capabilities of 3D scanning technologies, *Journal of Industrial Integration and Management* 8 (3) (2023) 321–339.
- [29] M.-G. Lee, Y. P. Korkolis, *Advances in plastic forming of metals* (2018).
- [30] L. Donati, B. Reggiani, R. Pelaccia, M. Negozio, S. Di Donato, Advancements in extrusion and drawing: a review of the contributes by the esaform community, *International Journal of Material Forming* 15 (3) (2022) 41.
- [31] G. Faraji, H. Torabzadeh, An overview on the continuous severe plastic deformation methods, *Materials transactions* 60 (7) (2019) 1316–1330.
- [32] A. Wu, Z. Zhang, Y. Xue, J. Xu, Research on material flow law and control for diffuence upsetting-extrusion forming of large-scale magnesium alloy complex housing, *Chinese Journal of Mechanical Engineering* 38 (1) (2025) 90.
- [33] U. Yoo, A. Hung, J. Francis, J. Oh, J. Ichnowski, Ropotter: Toward robotic pottery and deformable object manipulation with structural priors, in: *2024 IEEE-RAS 23rd International Conference on Humanoid Robots (Humanoids)*, IEEE, 2024, pp. 843–850.

- [34] A. Bartsch, A. B. Farimani, Planning and reasoning with 3D deformable objects for hierarchical Text-to-3D robotic shaping, *IEEE Robotics and Automation Letters* 10 (6) (2025) 6215–6222.